Frontiers of Information Technology & Electronic Engineering
www.jzus.zju.edu.cn; engineering.cae.cn; www.springerlink.com
ISSN 2095-9184 (print); ISSN 2095-9230 (online)
E-mail: jzus@zju.edu.cn



Analog-only beamforming for near-field multiuser MIMO communications*

Ying WANG[1,2], Chenhao QI‡[1,2]

[1]*School of Information Science and Engineering, Southeast University, Nanjing 210096, China*

[2]*National Mobile Communications Research Laboratory, Southeast University, Nanjing 210096, China*

E-mail: wying@seu.edu.cn; qch@seu.edu.cn

Received May 24, 2024; Revision accepted Oct. 15, 2024; Crosschecked Mar. 24, 2025

Abstract: For near-field multiuser communications based on hybrid beamforming (HBF) architectures, high-quality effective channel estimation is required to obtain the channel state information (CSI) for the design of the digital beamformer. To simplify the system reconfiguration and eliminate the pilot overhead required by effective channel estimation, we consider an analog-only beamforming (AoBF) architecture in this study. AoBF is designed to maximize the sum rate, it is transformed into a problem maximizing the power transmitted to the target user equipment (UE) and meanwhile minimizing the power leaked to the other UEs. To solve this problem, we use beam focusing and beam nulling and propose two AoBF schemes based on the majorization–minimization algorithm. First, the AoBF scheme based on perfect CSI is proposed, with the focus on beamforming performance and regardless of CSI acquisition. Then, the AoBF scheme based on imperfect CSI is proposed, where low-dimensional imperfect CSI is obtained by beam sweeping based on a near-field codebook. Simulation results demonstrate that the two AoBF schemes can approach HBF schemes in terms of the sum rate and outperform HBF schemes in terms of energy efficiency.

Key words: Beam focusing; Beamforming; Majorization–minimization; Multiuser communications; Near field
https://doi.org/10.1631/FITEE.2400433 **CLC number:** TN928

1 Introduction

Millimeter wave (mmWave) communications and terahertz (THz) communications are regarded as key technologies to support the very high data rate for future wireless communications. To deal with the serious path loss of signal propagation in these bands, large-scale antenna arrays are equipped at base stations (BSs) to improve the beam gain. Fortunately, the small wavelength of mmWave and THz wave allows the integration of more antennas on a small surface. However, the utilization of large-scale arrays enlarges the Rayleigh distance to dozens of meters, which makes the near-field effect not negligible. Different from far field, wireless propagation in the near field is precisely modeled as spherical waves instead of plane waves (Zhang et al., 2023; Chen et al., 2024). Thus, the near-field beam can be focused on a specific location, which is different from the far-field beam aligned to a certain angle regardless of distance (Wang J et al., 2024). Therefore, conventional far-field multiuser interference suppression methods may not be suitable for near-field multiuser communications (Alkhateeb et al., 2015).

To mitigate multiuser interference in the near field, various beamforming architectures are designed. The most flexible solution is the fully digital beamforming architecture (Zhang et al., 2022). However, this solution causes overwhelming hardware

‡ Corresponding author

* Project supported by the National Natural Science Foundation of China (Nos. U22B2007 and 62071116)

ORCID: Ying WANG, https://orcid.org/0000-0002-4541-9169; Chenhao QI, https://orcid.org/0000-0002-7360-939X

© Zhejiang University Press 2025

costs for large-scale multiple-input multiple-output (MIMO) systems since each antenna needs to be connected to a radio frequency (RF) chain. To deal with this problem, hybrid beamforming (HBF) architectures are widely used. An HBF scheme for near field is proposed to perform analog beamforming and digital beamforming alternatively until the HBF results approach the solutions of fully digital beamforming (Zhang et al., 2022). However, this scheme is designed based on the perfect knowledge of channel state information (CSI), which is impractical. One method is to estimate the near-field channels (Cui and Dai, 2022). Due to the equipped large-scale antenna arrays, the dimension of the channel matrix is high, and channel estimation is complex and challenging. To address this problem, beam sweeping is performed to obtain low-dimensional imperfect CSI. Based on the imperfect CSI obtained by beam sweeping, a two-stage HBF scheme is proposed for far-field communications (Alkhateeb et al., 2015). In the first stage of this scheme, analog beamforming is designed according to the code word selected by beam sweeping, and then the effective channel (Sun XY et al., 2019) is estimated. In the second stage, digital beamforming is designed based on the effective channel to mitigate multiuser interference. This two-stage HBF method is extended to the near field (Wu ZD and Dai, 2023). To simplify the system reconfiguration and eliminate the pilot overhead required by effective channel estimation, in this study, we consider using the analog-only beamforming (AoBF) architecture to replace HBF. Similar to the reconfigurable intelligent surface (RIS) composed of passive reflecting elements (Tian et al., 2022, 2024; Liu et al., 2023; Wang XH et al., 2023; Yang et al., 2023), AoBF can flexibly adjust the beam pattern only relying on phase shifters. As shown in Fig. 1, the AoBF architecture omits the digital beamforming module. The removal of the digital beamforming module can improve the energy efficiency (Cao et al., 2017; Shen et al., 2024). Note that AoBF can be adopted by the BS to simplify the system reconfiguration, while the RIS is typically placed between the BS and the user equipment (UE) to provide an additional propagation path for the wireless signal (You and Zhang, 2021; Li et al., 2024). Besides, the architectures of AoBF and RIS are different considering the deployment of RF chains, where the RF chain includes mixers, analog-to-digital converters (ADCs) or digital-to-analog converters (DACs), and date converters (Ahmed et al., 2018). These components are necessary for the BS but are not included in the RIS. To reduce the pilot overhead, an AoBF scheme based on the majorization–minimization (MM) method is proposed for partially connected mmWave MIMO in the far field, which is named A-MM (Qi et al., 2024). However, this far-field scheme cannot be directly extended to near-field communications due to

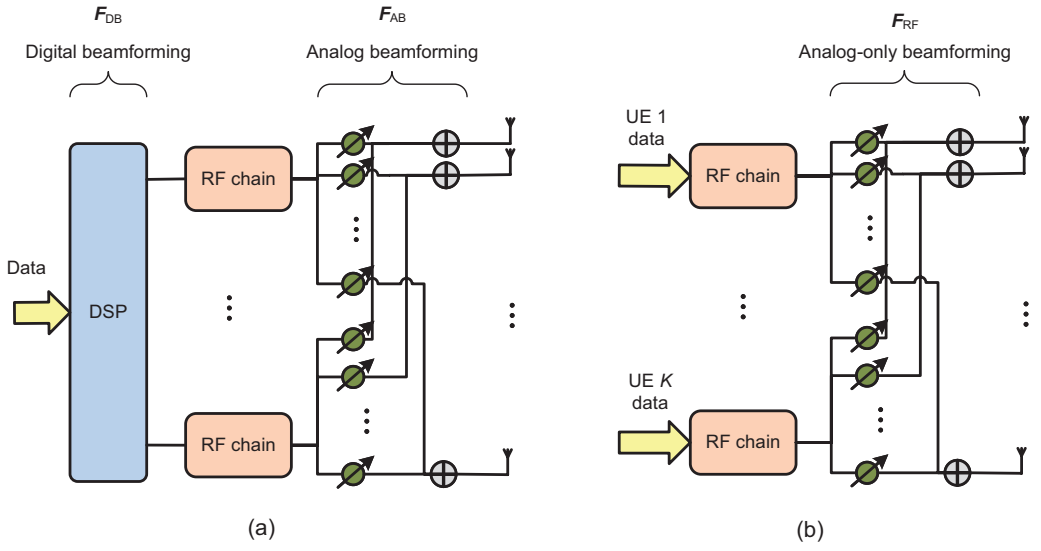


Fig. 1 Beamforming architecture comparison: (a) HBF architecture; (b) AoBF architecture. HBF: hybrid beamforming; AoBF: analog-only beamforming; DSP: digital signal processing; RF: radio frequency; UE: user equipment

the inappropriateness of channel modeling and codebook design.

In this study, we consider AoBF for near-field multiuser MIMO systems. AoBF is designed to maximize the sum rate, it is transformed into a problem maximizing the power transmitted to the target UE and meanwhile minimizing the power leaked to the other UEs. To solve this problem, we use beam focusing and beam nulling and propose two AoBF schemes based on the MM algorithm. First, the AoBF scheme based on perfect CSI is proposed to show the feasibility of replacing HBF with AoBF in the near field, with the focus on beamforming performance and regardless of CSI acquisition. Then, the AoBF scheme based on imperfect CSI is proposed to meet the practical requirement, where low-dimensional imperfect CSI is obtained by beam sweeping based on a near-field codebook. Since the best code word from beam sweeping corresponds to an area rather than an accurate location, we propose a heuristic method to approximate the channel vector by generating auxiliary points within the area.

Notations: Symbols for vectors (lower case) and matrices (upper case) are in boldface. $\mathbb{C}$ and $\mathbb{R}$ denote the sets of complex- and real-valued numbers, respectively. For a vector $\boldsymbol{a}$, $\|\boldsymbol{a}\|_2$ and $[\boldsymbol{a}]_n$ denote the l_2-norm and the n^{th} entry, respectively. For a matrix $\boldsymbol{A}$, $[\boldsymbol{A}]_{m,:}$, $[\boldsymbol{A}]_{:,n}$, $[\boldsymbol{A}]_{m,n}$, and $\boldsymbol{A}^{\text{H}}$ denote the m^{th} row, the n^{th} column, the entry at the m^{th} row and n^{th} column, and the conjugate transpose (Hermitian), respectively. $\Re\{\cdot\}$ denotes the real part of a complex-valued number. $\angle(\cdot)$ denotes the phase of a complex-valued number. $\mathcal{CN}(0,\sigma^2)$ denotes the complex Gaussian distribution with zero mean and σ^2 variance.

2 System model

Considering the downlink transmission for the multiuser MIMO system in the near field, the BS is equipped with N_{BS} antennas in terms of uniform linear arrays (ULAs) and serves K UEs simultaneously. The number of UEs served simultaneously is restricted by the number of RF chains at the BS, i.e., $K \le N_{\text{RF}}$. For simplicity, we assume that the RF chains are fully used in this study, i.e., $K = N_{\text{RF}}$. The origin $(0,0)$ of the XY-plane is assumed to be located at the center of the ULA, as shown in Fig. 2. The location of the k^{th} UE is denoted as (x_k, y_k) in Cartesian coordinates. The conversion between Cartesian and polar coordinates can be expressed as follows:

$$(\varphi_k, \rho_k) = \left(\arctan\frac{x_k}{y_k}, \sqrt{x_k^2+y_k^2}\right), \tag{1a}$$

$$(x_k, y_k) = (\rho_k \sin\varphi_k, \rho_k \cos\varphi_k). \tag{1b}$$

Given the wavelength λ of signals and the adjacent distance between antennas $d = \lambda/2$, the n^{th} antenna in the ULA is located at $(d\gamma_n, 0)$, where $\gamma_n \triangleq n - (N_{\text{BS}}+1)/2, n = 1, 2, \ldots, N_{\text{BS}}$. The distance between the k^{th} UE and the n^{th} antenna can be computed by (Cui and Dai, 2024)

$$\begin{aligned}\rho_{(n)}(\varphi_k,\rho_k) =& \sqrt{(x_k - d\gamma_n)^2 + y_k^2} \\ =& \sqrt{\rho_k^2 + d^2\gamma_n^2 - 2d\gamma_n\rho_k\sin\varphi_k}.\end{aligned} \tag{2}$$

Then, the channel steering vector in the near field is defined as

$$\begin{aligned}&\boldsymbol{u}(\varphi_k,\rho_k) \\ &\triangleq \frac{1}{\sqrt{N_{\text{BS}}}}\left[\mathrm{e}^{\frac{-\mathrm{j}2\pi\rho_{(1)}(\varphi_k,\rho_k)}{\lambda}}, \ldots, \mathrm{e}^{\frac{-\mathrm{j}2\pi\rho_{(N_{\text{BS}})}(\varphi_k,\rho_k)}{\lambda}}\right]^{\text{T}}.\end{aligned} \tag{3}$$

As shown in Fig. 2a, the distance in the far field under the plane wave assumption can be simplified as (Cui and Dai, 2024)

$$\begin{aligned}\rho_{(n)}(\varphi_k,\rho_k) =& \rho_k\left(1 + \frac{d^2\gamma_n^2}{\rho_k^2} - \frac{2d\gamma_n\sin\varphi_k}{\rho_k}\right)^{\frac{1}{2}} \\ \approx& \rho_k\left(1 - \frac{d\gamma_n\sin\varphi_k}{\rho_k}\right) \\ =& \rho_k - d\gamma_n\sin\varphi_k,\end{aligned} \tag{4}$$

where $(d^2\gamma_n^2)/\rho_k^2$ is ignored since $\rho_k \gg d$ in the far field, and then the approximation is performed according to the first-order Taylor expansion $(1+x)^{1/2} \approx 1 + x/2$. By ignoring the constant phase independent of n, the channel steering vector in the far field can be denoted as $\boldsymbol{u}'(\varphi_k) \triangleq \frac{1}{\sqrt{N_{\text{BS}}}}\left[\mathrm{e}^{-\mathrm{j}2\pi d\sin\varphi_k/\lambda}, \ldots, \mathrm{e}^{-\mathrm{j}2\pi N_{\text{BS}} d\sin\varphi_k/\lambda}\right]^{\text{T}}$, whose phases are linear to the antenna index n. Note that the far-field steering vector is related only to the angle of the UE, regardless of the distance. In the near field, the assumption $\rho_k \gg d$ does not hold anymore, and the approximation based on Taylor expansion is not accurate when n is large. Thus, the plane wave assumption in Eq. (4) fails in the near field. On the contrary, the near-field steering vector in Eq. (3) is

related to both the angle and the distance. The introduction of the distance dimension provides more degrees of freedom for beamforming.

Within the Rayleigh distance (Sherman, 1962) $D_{\mathrm{R}} \triangleq 2N_{\mathrm{BS}}^2 d^2/\lambda$, as shown in Fig. 2b, the near-field spherical-wave channel model (Cui and Dai, 2022) for the k^{th} UE is denoted as

$$\boldsymbol{h}_k = \sqrt{\frac{N_{\mathrm{BS}}}{L}} \sum_{l=1}^{L} \alpha_{k,l} \boldsymbol{u}\left(\varphi_{k,l}, \rho_{k,l}\right), \tag{5}$$

where L, $\alpha_{k,l}$, and $(\varphi_{k,l}, \rho_{k,l})$ are the number of channel paths, the complex channel gain of the l^{th} path, for $l = 1, 2, \ldots, L$, and the polar coordinates of the UE or scatterers, respectively. Note that, in this study, we design the scheme based on mathematically abstracted channel modeling for the convenience of signal processing and system analysis (Gong TR et al., 2024c). However, the proposed scheme can be extended to physically consistent modeling (PCM) to consider the physical effects of wave propagation (Gong TR et al., 2024a, 2024b, 2024c). In our future work, we will investigate AoBF based on PCM. Given the channel model $\boldsymbol{h}_k$ in Eq. (5), the signal received at the k^{th} UE is denoted as

$$y_k = \sqrt{P}\boldsymbol{h}_k^{\mathrm{H}} \boldsymbol{F}\boldsymbol{x} + n_k, \tag{6}$$

where $\boldsymbol{F} \in \mathbb{C}^{N_{\mathrm{BS}} \times K}$, $\boldsymbol{x} \in \mathbb{C}^K$, y_k, and n_k denote the beamforming matrix at the BS, the signals transmitted to K UEs, the received signal, and an additive white Gaussian noise (AWGN) with zero mean and σ^2 variance, i.e., $n_k \sim \mathcal{CN}\left(0, \sigma^2\right)$, respectively. In addition, the total power of the BS is P, and the transmitted signals are subject to the unit power constraint, i.e., $\mathbb{E}\{\boldsymbol{x}\boldsymbol{x}^{\mathrm{H}}\} = \boldsymbol{I}_K$.

To maximize the sum rate of near-field multiuser MIMO, the beamforming design problem is formulated as

$$\begin{aligned} &\max_{\boldsymbol{F}} \sum_{k=1}^{K} R_k \\ &\text{s.t.} \quad \|\boldsymbol{F}\|_{\mathrm{F}} = K, \end{aligned} \tag{7}$$

where the achievable rate of the k^{th} UE can be computed by

$$R_k \triangleq \log_2\left(1 + \mathrm{SINR}_k\right), \tag{8a}$$

$$\mathrm{SINR}_k \triangleq \frac{\frac{P}{K}\left|\boldsymbol{h}_k^{\mathrm{H}}\left[\boldsymbol{F}\right]_{:,k}\right|^2}{\frac{P}{K}\sum\limits_{i\neq k}^{K}\left|\boldsymbol{h}_k^{\mathrm{H}}\left[\boldsymbol{F}\right]_{:,i}\right|^2 + \sigma^2}. \tag{8b}$$

Note that SINR_k represents the signal-to-interference-plus-noise ratio (SINR) for the k^{th} UE. Particularly, maximizing the sum rate in Eq. (7) is equivalent to maximizing the SINR of each UE. Thus, we can transform problem (7) into K subproblems as

$$\begin{aligned} &\max_{\boldsymbol{F}} \mathrm{SINR}_k \\ &\text{s.t.} \quad \left\|\boldsymbol{F}\right\|_{\mathrm{F}} = K. \end{aligned} \tag{9}$$

During the downlink transmission, the BS designs $\boldsymbol{F}$ to maximize the sum rate.

For HBF schemes, as shown in Fig. 1a, HBF is implemented by the combination of analog beamforming and digital beamforming (Wu ZD and Dai, 2023), i.e., $\boldsymbol{F} \triangleq \boldsymbol{F}_{\mathrm{AB}}\boldsymbol{F}_{\mathrm{DB}}$. Analog beamforming is denoted as $\boldsymbol{F}_{\mathrm{AB}} \triangleq [\boldsymbol{v}_{(1)}, \boldsymbol{v}_{(2)}, \ldots, \boldsymbol{v}_{(K)}]$, where each code word $\boldsymbol{v}_{(k)} \in \mathbb{C}^{N_{\mathrm{BS}}}$ with the constant modulus constraint $\left|[\boldsymbol{v}_{(k)}]_n\right| = 1/\sqrt{N_{\mathrm{BS}}}$ is determined by beam sweeping and implemented by phase

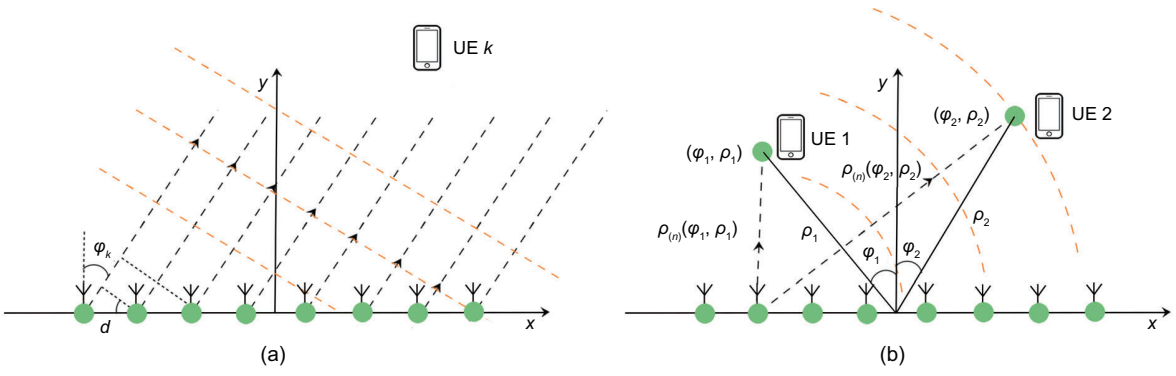


Fig. 2 The channel models in the far field (a) and the near field (b)

shifters (Alkhateeb et al., 2015). Then, the effective channel $\widetilde{\boldsymbol{h}}_k = \boldsymbol{F}_{\mathrm{AB}}^{\mathrm{H}}\boldsymbol{h}_k$ can be obtained by pilot-assisted channel estimation. Based on $\widetilde{\boldsymbol{h}}_k$, digital beamforming $\boldsymbol{F}_{\mathrm{DB}}$ can be designed via zero forcing (ZF) or weighted minimum mean-squared error (WMMSE) with the constraint $\left\|\boldsymbol{F}_{\mathrm{AB}}[\boldsymbol{F}_{\mathrm{DB}}]_{:,k}\right\|_{\mathrm{F}}=1$. This constraint means that HBF provides no power gain.

For our AoBF scheme, $\boldsymbol{F}$ is designed merely by analog beamforming, i.e., $\boldsymbol{F} \triangleq \boldsymbol{F}_{\mathrm{RF}}$, as shown in Fig. 1b. Thus, the pilot overhead required by effective channel estimation in the HBF schemes can be omitted. AoBF is denoted as $\boldsymbol{F}_{\mathrm{RF}} \in \mathbb{C}^{N_{\mathrm{BS}}\times K}$ with the constant modulus constraint $|[\boldsymbol{F}_{\mathrm{RF}}]_{n,k}| = 1/\sqrt{N_{\mathrm{BS}}}$. We design the phase of each entry in $\boldsymbol{F}_{\mathrm{RF}}$ to maximize the sum rate.

3 AoBF for near-field multiuser MIMO

To simplify the system reconfiguration and eliminate the pilot overhead required by effective channel estimation, we consider the AoBF architecture in this study. In this section, we propose two AoBF schemes for near-field multiuser MIMO by exploiting the extra degree of freedom in the distance domain provided from spherical waves. The AoBF scheme based on perfect CSI is first proposed to show the feasibility of replacing HBF with AoBF in the near field, with the focus on beamforming performance and regardless of CSI acquisition. Then, the AoBF scheme based on imperfect CSI is designed to meet the practical requirement where low-dimensional imperfect CSI is obtained by beam sweeping based on a near-field codebook.

3.1 AoBF based on perfect CSI

With the focus on beamforming performance and regardless of CSI acquisition, we assume that the CSI is perfectly known. As analog beamforming for all UEs is coupled in Eq. (8b), the signal-to-leakage-and-noise ratio (SLNR) is applied to replace SINR for decoupling in this study (Gong SQ et al., 2020). The expression of SLNR in AoBF is denoted as follows:

$$\mathrm{SLNR}_k \triangleq \frac{\frac{P}{K}\left|\boldsymbol{h}_k^{\mathrm{H}}\left[\boldsymbol{F}_{\mathrm{RF}}\right]_{:,k}\right|^2}{\frac{P}{K}\sum\limits_{i\neq k}^{K}\left|\boldsymbol{h}_i^{\mathrm{H}}\left[\boldsymbol{F}_{\mathrm{RF}}\right]_{:,k}\right|^2+\sigma^2}. \tag{10}$$

Note that the difference between the SINR in Eq. (8b) and the SLNR in Eq. (10) lies in the interference term in the denominator. For SINR_k, $\sum\limits_{i\neq k}^{K}\left|\boldsymbol{h}_k^{\mathrm{H}}\left[\boldsymbol{F}_{\mathrm{RF}}\right]_{:,i}\right|^2$ denotes the power of interference from all other UEs to the target UE, i.e., the k^{th} UE. For SLNR_k, $\sum\limits_{i\neq k}^{K}\left|\boldsymbol{h}_i^{\mathrm{H}}\left[\boldsymbol{F}_{\mathrm{RF}}\right]_{:,k}\right|^2$ represents the power leaked from the target UE to all the other UEs. Reducing the interference power from the other UEs to the target UE and mitigating the leaked power from the target UE to the other UEs are intrinsically equivalent for multiuser interference suppression. Thus, the optimization problem (9) can be converted into

$$\begin{aligned}&\max_{[\boldsymbol{F}_{\mathrm{RF}}]_{:,k}}\ \mathrm{SLNR}_k\\ &\text{s.t.}\ \ \left|[\boldsymbol{F}_{\mathrm{RF}}]_{n,k}\right|=\frac{1}{\sqrt{N_{\mathrm{BS}}}}.\end{aligned} \tag{11}$$

To simplify problem (11), a weight parameter ω is introduced to the optimization, and the constant term $\omega\sigma^2K/P$ is removed for its independence of $[\boldsymbol{F}_{\mathrm{RF}}]_{:,k}$. The objective function of the simplified problem can be expressed as

$$\min_{[\boldsymbol{F}_{\mathrm{RF}}]_{:,k}}\Big(-\left|\boldsymbol{h}_k^{\mathrm{H}}\left[\boldsymbol{F}_{\mathrm{RF}}\right]_{:,k}\right|^2+\omega\sum_{i\neq k}^{K}\left|\boldsymbol{h}_i^{\mathrm{H}}\left[\boldsymbol{F}_{\mathrm{RF}}\right]_{:,k}\right|^2\Big). \tag{12}$$

The original problem (7) is transformed into problem (12), maximizing the power focused on the target UE and meanwhile minimizing the power leaked to the other UEs. To solve this non-convex problem, we use beam focusing and beam nulling based on the MM method (Gong SQ et al., 2020). The MM method is an iterative algorithm, with each iteration consisting of a majorization stage and a minimization stage. In the majorization stage, the original non-convex objective function is transformed into a surrogate function that is easy to optimize at the feasible point. The feasible point is obtained from the initialization or the last iteration. This surrogate function serves as an upper-bound function with the same value and derivative as the original function at the feasible point. Then, in the minimization stage, the surrogate function is minimized to update the feasible point. Owing to the closed-form solutions to the surrogate functions, the iterations achieve rapid convergence (Sun Y et al., 2017; Wu LL et al., 2018; Gong SQ et al., 2020).

Since the first term in expression (12) is concave, we have

$$\begin{aligned}
&-\left|\boldsymbol{h}_k^{\mathrm{H}}\left[\boldsymbol{F}_{\mathrm{RF}}\right]_{:,k}\right|^2\\
=&-\left[\boldsymbol{F}_{\mathrm{RF}}\right]_{:,k}^{\mathrm{H}}\boldsymbol{h}_k\boldsymbol{h}_k^{\mathrm{H}}\left[\boldsymbol{F}_{\mathrm{RF}}\right]_{:,k}\\
\leq&-([\boldsymbol{F}_{\mathrm{RF}}]_{:,k}^{(t)})^{\mathrm{H}}\boldsymbol{h}_k\boldsymbol{h}_k^{\mathrm{H}}\left[\boldsymbol{F}_{\mathrm{RF}}\right]_{:,k}^{(t)}\\
&-2\left(\boldsymbol{h}_k\boldsymbol{h}_k^{\mathrm{H}}\left[\boldsymbol{F}_{\mathrm{RF}}\right]_{:,k}^{(t)}\right)^{\mathrm{H}}\left(\left[\boldsymbol{F}_{\mathrm{RF}}\right]_{:,k}-\left[\boldsymbol{F}_{\mathrm{RF}}\right]_{:,k}^{(t)}\right)\\
=&-2\left(\boldsymbol{h}_k\boldsymbol{h}_k^{\mathrm{H}}\left[\boldsymbol{F}_{\mathrm{RF}}\right]_{:,k}^{(t)}\right)^{\mathrm{H}}\left[\boldsymbol{F}_{\mathrm{RF}}\right]_{:,k}+c_1,
\end{aligned}\tag{13}$$

where $[\boldsymbol{F}_{\mathrm{RF}}]_{:,k}^{(t)}$ is the feasible point obtained in the t^{th} iteration and c_1 is a constant independent of $[\boldsymbol{F}_{\mathrm{RF}}]_{:,k}$. Since $\left|\boldsymbol{h}_k^{\mathrm{H}}\left[\boldsymbol{F}_{\mathrm{RF}}\right]_{:,k}\right|^2$ is real-valued, we can obtain $\Re\Big\{-\left|\boldsymbol{h}_k^{\mathrm{H}}\left[\boldsymbol{F}_{\mathrm{RF}}\right]_{:,k}\right|^2\Big\}=-\left|\boldsymbol{h}_k^{\mathrm{H}}\left[\boldsymbol{F}_{\mathrm{RF}}\right]_{:,k}\right|^2$. Thus, if we obtain the real value of both sides in (13), we have

$$-\left|\boldsymbol{h}_k^{\mathrm{H}}\left[\boldsymbol{F}_{\mathrm{RF}}\right]_{:,k}\right|^2\leq-2\Re\{\left[\boldsymbol{F}_{\mathrm{RF}}\right]_{:,k}^{\mathrm{H}}\boldsymbol{h}_k\boldsymbol{h}_k^{\mathrm{H}}\left[\boldsymbol{F}_{\mathrm{RF}}\right]_{:,k}^{(t)}\}+c_1,\tag{14}$$

where

$$\begin{aligned}
&\Re\left\{\left(\boldsymbol{h}_k\boldsymbol{h}_k^{\mathrm{H}}\left[\boldsymbol{F}_{\mathrm{RF}}\right]_{:,k}^{(t)}\right)^{\mathrm{H}}\left[\boldsymbol{F}_{\mathrm{RF}}\right]_{:,k}\right\}\\
=&\Re\{\left[\boldsymbol{F}_{\mathrm{RF}}\right]_{:,k}^{\mathrm{H}}\boldsymbol{h}_k\boldsymbol{h}_k^{\mathrm{H}}\left[\boldsymbol{F}_{\mathrm{RF}}\right]_{:,k}^{(t)}\}.
\end{aligned}\tag{15}$$

Based on Lemma 1 proposed by Song et al. (2015), each entry of the second term in (12) satisfies

$$\begin{aligned}
&\left|\boldsymbol{h}_i^{\mathrm{H}}\left[\boldsymbol{F}_{\mathrm{RF}}\right]_{:,k}\right|^2\\
=&\left[\boldsymbol{F}_{\mathrm{RF}}\right]_{:,k}^{\mathrm{H}}\boldsymbol{h}_i\boldsymbol{h}_i^{\mathrm{H}}\left[\boldsymbol{F}_{\mathrm{RF}}\right]_{:,k}\\
\leq&\left(\left[\boldsymbol{F}_{\mathrm{RF}}\right]_{:,k}^{(t)}\right)^{\mathrm{H}}\boldsymbol{h}_i\boldsymbol{h}_i^{\mathrm{H}}\left[\boldsymbol{F}_{\mathrm{RF}}\right]_{:,k}^{(t)}\\
&+\mu\left(\left[\boldsymbol{F}_{\mathrm{RF}}\right]_{:,k}-\left[\boldsymbol{F}_{\mathrm{RF}}\right]_{:,k}^{(t)}\right)^{\mathrm{H}}\left(\left[\boldsymbol{F}_{\mathrm{RF}}\right]_{:,k}-\left[\boldsymbol{F}_{\mathrm{RF}}\right]_{:,k}^{(t)}\right)\\
&+2\Re\left\{\left(\left[\boldsymbol{F}_{\mathrm{RF}}\right]_{:,k}-\left[\boldsymbol{F}_{\mathrm{RF}}\right]_{:,k}^{(t)}\right)^{\mathrm{H}}\boldsymbol{h}_i\boldsymbol{h}_i^{\mathrm{H}}\left[\boldsymbol{F}_{\mathrm{RF}}\right]_{:,k}^{(t)}\right\}\\
=&\mu\left[\boldsymbol{F}_{\mathrm{RF}}\right]_{:,k}^{\mathrm{H}}\left[\boldsymbol{F}_{\mathrm{RF}}\right]_{:,k}\\
&+\left(\left[\boldsymbol{F}_{\mathrm{RF}}\right]_{:,k}^{(t)}\right)^{\mathrm{H}}\left(\mu\boldsymbol{I}_{N_{\mathrm{BS}}}-\boldsymbol{h}_i\boldsymbol{h}_i^{\mathrm{H}}\right)\left[\boldsymbol{F}_{\mathrm{RF}}\right]_{:,k}^{(t)}\\
&+2\Re\left\{\left[\boldsymbol{F}_{\mathrm{RF}}\right]_{:,k}^{\mathrm{H}}\left(\boldsymbol{h}_i\boldsymbol{h}_i^{\mathrm{H}}-\mu\boldsymbol{I}_{N_{\mathrm{BS}}}\right)\left[\boldsymbol{F}_{\mathrm{RF}}\right]_{:,k}^{(t)}\right\}\\
=&2\Re\left\{\left[\boldsymbol{F}_{\mathrm{RF}}\right]_{:,k}^{\mathrm{H}}\left(\boldsymbol{h}_i\boldsymbol{h}_i^{\mathrm{H}}-\mu\boldsymbol{I}_{N_{\mathrm{BS}}}\right)\left[\boldsymbol{F}_{\mathrm{RF}}\right]_{:,k}^{(t)}\right\}+c_2,
\end{aligned}\tag{16}$$

where c_2, $\boldsymbol{I}_{N_{\mathrm{BS}}}\in\mathbb{C}^{N_{\mathrm{BS}}\times N_{\mathrm{BS}}}$, and μ denote a constant independent of $[\boldsymbol{F}_{\mathrm{RF}}]_{:,k}$, a unit diagonal matrix, and the maximum eigenvalue of the one-rank matrix $\boldsymbol{h}_i\boldsymbol{h}_i^{\mathrm{H}}$, respectively. Thus, we can obtain

$$\begin{aligned}
&\sum_{i\neq k}^{K}\left|\boldsymbol{h}_i^{\mathrm{H}}\left[\boldsymbol{F}_{\mathrm{RF}}\right]_{:,k}\right|^2\\
\leq&2\Re\left\{\left[\boldsymbol{F}_{\mathrm{RF}}\right]_{:,k}^{\mathrm{H}}\sum_{i\neq k}^{K}\left(\boldsymbol{h}_i\boldsymbol{h}_i^{\mathrm{H}}-\mu\boldsymbol{I}_{N_{\mathrm{BS}}}\right)\left[\boldsymbol{F}_{\mathrm{RF}}\right]_{:,k}^{(t)}\right\}+c_3,
\end{aligned}\tag{17}$$

where $c_3\triangleq(K-1)c_2$. By adding the corresponding sides of inequalities (14) and (17), we have

$$\begin{aligned}
&-\left|\boldsymbol{h}_k^{\mathrm{H}}\left[\boldsymbol{F}_{\mathrm{RF}}\right]_{:,k}\right|^2+\omega\sum_{i\neq k}^{K}\left|\boldsymbol{h}_i^{\mathrm{H}}\left[\boldsymbol{F}_{\mathrm{RF}}\right]_{:,k}\right|^2\\
\leq&2\Re\left\{\left[\boldsymbol{F}_{\mathrm{RF}}\right]_{:,k}^{\mathrm{H}}\left(-\boldsymbol{\Pi}_1^{(t)}+\omega\boldsymbol{\Pi}_2^{(t)}\right)\left[\boldsymbol{F}_{\mathrm{RF}}\right]_{:,k}^{(t)}\right\}+c_4,
\end{aligned}\tag{18}$$

where

$$\boldsymbol{\Pi}_1^{(t)}\triangleq\boldsymbol{h}_k\boldsymbol{h}_k^{\mathrm{H}},\tag{19a}$$

$$\boldsymbol{\Pi}_2^{(t)}\triangleq\sum_{i\neq k}^{K}\left(\boldsymbol{h}_i\boldsymbol{h}_i^{\mathrm{H}}-\mu\boldsymbol{I}_{N_{\mathrm{BS}}}\right),\tag{19b}$$

$$c_4\triangleq c_1+c_3.\tag{19c}$$

The right part of inequality (18) is an available surrogate function of the original objective function (12). By ignoring constant variable c_4 and multiplier 2, problem (12) can be rewritten as

$$\min_{[\boldsymbol{F}_{\mathrm{RF}}]_{:,k}}\Re\left\{\left[\boldsymbol{F}_{\mathrm{RF}}\right]_{:,k}^{\mathrm{H}}\left(-\boldsymbol{\Pi}_1^{(t)}+\omega\boldsymbol{\Pi}_2^{(t)}\right)\left[\boldsymbol{F}_{\mathrm{RF}}\right]_{:,k}^{(t)}\right\}.\tag{20}$$

Based on $\|\boldsymbol{a}-\boldsymbol{b}\|_{\mathrm{F}}^2=\|\boldsymbol{a}\|_{\mathrm{F}}^2+\|\boldsymbol{b}\|_{\mathrm{F}}^2-2\Re\{\boldsymbol{a}^{\mathrm{H}}\boldsymbol{b}\}$, problem (20) can be rewritten as follows:

$$\max_{[\boldsymbol{F}_{\mathrm{RF}}]_{:,k}}\left\|\left[\boldsymbol{F}_{\mathrm{RF}}\right]_{:,k}^{\mathrm{H}}+\left(\boldsymbol{\Pi}_1^{(t)}-\omega\boldsymbol{\Pi}_2^{(t)}\right)\left[\boldsymbol{F}_{\mathrm{RF}}\right]_{:,k}^{(t)}\right\|_{\mathrm{F}}^2.\tag{21}$$

Due to the constant modulus constraint and the property of vectors, the closed-form solution to problem (21) is expressed as

$$\left[\boldsymbol{F}_{\mathrm{RF}}\right]_{n,k}^{(t+1)}=\mathrm{e}^{\mathrm{j}\angle\left(\left[\left(\boldsymbol{\Pi}_i^{(t)}-\omega\boldsymbol{\Pi}_2^{(t)}\right)\left[\boldsymbol{F}_{\mathrm{RF}}\right]_{:,k}^{(t)}\right]_n\right)}.\tag{22}$$

The details of the AoBF scheme based on perfect CSI are exhibited in Algorithm 1. The stop condition in step 11 is set as $\left\|\left[\boldsymbol{F}_{\mathrm{RF}}\right]_{:,k}^{(t)}-\left[\boldsymbol{F}_{\mathrm{RF}}\right]_{:,k}^{(t-1)}\right\|_2^2\leq\epsilon$ or $t>T_{\max}$.

3.2 AoBF based on imperfect CSI

In practice, the perfect CSI is unknown, and the estimation of high-dimensional CSI is challenging.

Algorithm 1 AoBF based on perfect CSI

Input: N_{BS}, $\boldsymbol{h}_k$, ω, ϵ, and $T_{\max}$.
for $k=1:K$ **do**
  for $n=1:N_{\mathrm{BS}}$ **do**
    Initialize $[\boldsymbol{F}_{\mathrm{RF}}]_{n,k}^{(t)}=\frac{1}{\sqrt{N_{\mathrm{BS}}}}\mathrm{e}^{\mathrm{j}\angle([\boldsymbol{h}_k]_n)}$, $t=0$
  end for
  repeat
    Obtain $\boldsymbol{\Pi}_1^{(t)}$ via Eq. (19a)
    Obtain $\boldsymbol{\Pi}_2^{(t)}$ via Eq. (19b)
    Obtain $[\boldsymbol{F}_{\mathrm{RF}}]_{:,k}^{(t+1)}$ via Eq. (22)
    $t=t+1$
  until stop condition is satisfied
  $[\boldsymbol{F}_{\mathrm{RF}}]_{:,k}=[\boldsymbol{F}_{\mathrm{RF}}]_{:,k}^{(t)}$
end for
Output: $\boldsymbol{F}_{\mathrm{RF}}$.

Normally, to address this problem, beam sweeping is performed to obtain low-dimensional imperfect CSI (Yoon and Lee, 2022). For near-field beam sweeping, the space is scanned in both the angle and distance dimensions based on a polar-domain near-field codebook $\boldsymbol{\mathcal{V}}$ (Cui and Dai, 2022). The $(p,q)^{\mathrm{th}}$ code word of $\boldsymbol{\mathcal{V}}$ is given by

$$\begin{cases}\boldsymbol{v}_{p,q}\triangleq\boldsymbol{u}(\bar{\varphi}_p,\bar{\rho}_{p,q}),\\ \bar{\varphi}_p\triangleq\arcsin\left(\dfrac{2p-1}{N_{\mathrm{BS}}}-1\right),\quad p=1,2,\ldots,N_{\mathrm{BS}},\\ \bar{\rho}_{p,q}\triangleq\dfrac{N_{\mathrm{BS}}^2d^2}{2q\beta_{\Delta}^2\lambda}\left\{1-\sin^2\varphi_p\right\},\quad q=1,2,\ldots,N_{\mathrm{DIS}},\end{cases}\tag{23}$$

where p and q are the indices in angle and distance dimensions respectively, β_{Δ} is a parameter related to the correlation between adjacent code words at the same angle, and N_{DIS} represents the total number of indices in the distance dimension (Cui and Dai, 2022).

Since the best code word selected by near-field beam sweeping corresponds to an area rather than an accurate location, we propose a heuristic method to approximate the unknown $\boldsymbol{h}_k$ by generating auxiliary points within the area (Fig. 3). The numbers of auxiliary points in the angle and distance dimensions are denoted as R and S, respectively. The index of the best code word selected by beam sweeping for the k^{th} UE is denoted as $(\widetilde{p}_k,\widetilde{q}_k)$. Thus, the angle of the $(r,s)^{\mathrm{th}}$ auxiliary point in the corresponding area is denoted as

$$\begin{cases}\widehat{\varphi}_{k,r}\triangleq\arcsin\left(\dfrac{2\widehat{p}_{k,r}-1}{RN_{\mathrm{BS}}}-1\right),\\ \widehat{p}_{k,r}\triangleq R(\widetilde{p}_k-1)+r,\\ r=1,2,\ldots,R.\end{cases}\tag{24}$$

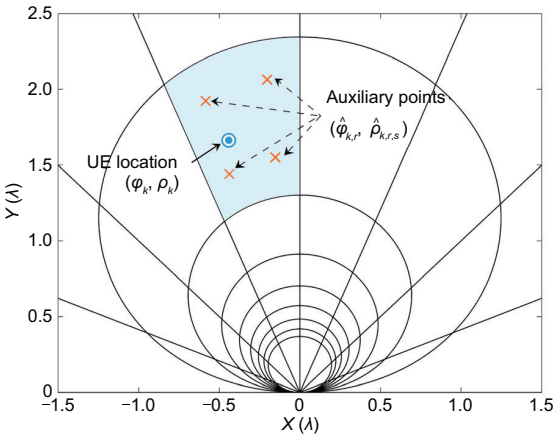


Fig. 3 Illustration of beam sweeping code words and auxiliary points

The distance of the $(r,s)^{\mathrm{th}}$ auxiliary point is denoted as

$$\begin{cases}\widehat{\rho}_{k,r,s}\triangleq\dfrac{N_{\mathrm{BS}}^2d^2}{2\widehat{q}_{k,s}\beta_{\Delta}^2\lambda}\left(1-\sin^2\widehat{\varphi}_{k,r}\right),\\ \widehat{q}_{k,s}\triangleq\dfrac{4S}{2S\left(\frac{1}{\widetilde{q}_k}+\frac{1}{\widetilde{q}_k+1}\right)+\left(\frac{1}{\widetilde{q}_k-1}-\frac{1}{\widetilde{q}_k+1}\right)(2s-1)},\\ s=1,2,\ldots,S.\end{cases}\tag{25}$$

Then, the steering vectors corresponding to the auxiliary points within the area are used to approximate $\boldsymbol{h}_k$, and the objective function (11) can be transformed into

$$\max_{[\boldsymbol{F}_{\mathrm{RF}}]_{:,k}}\frac{\dfrac{1}{RS}\displaystyle\sum_{r=1}^{R}\sum_{s=1}^{S}\left|\boldsymbol{u}^{\mathrm{H}}(\widehat{\varphi}_{k,r},\widehat{\rho}_{k,r,s})\,[\boldsymbol{F}_{\mathrm{RF}}]_{:,k}\right|^2}{\dfrac{1}{RS}\displaystyle\sum_{i\neq k}^{K}\sum_{r=1}^{R}\sum_{s=1}^{S}\left|\boldsymbol{u}^{\mathrm{H}}(\widehat{\varphi}_{i,r},\widehat{\rho}_{i,r,s})\,[\boldsymbol{F}_{\mathrm{RF}}]_{:,k}\right|^2+\sigma^2}.\tag{26}$$

Note that the generation of auxiliary points introduces no extra overhead to the scheme since it is a pure calculation process rather than a sampling operation in the space. Then, the MM algorithm is used to solve problem (26). The closed-form solution in the t^{th} iteration of MM optimization can be denoted as

$$[\boldsymbol{F}_{\mathrm{RF}}]_{n,k}^{(t+1)}=\mathrm{e}^{\mathrm{j}\angle\left(\left[\left(\boldsymbol{\Omega}_i^{(t)}-\omega\boldsymbol{\Omega}_2^{(t)}\right)[\boldsymbol{F}_{\mathrm{RF}}]_{:,k}^{(t)}\right]_n\right)},\tag{27}$$

where

$$\boldsymbol{\Omega}_1^{(t)} \triangleq \sum_{r=1}^{R}\sum_{s=1}^{S} \boldsymbol{u}(\widehat{\varphi}_{k,r},\widehat{\rho}_{k,r,s})\boldsymbol{u}^{\mathrm{H}}(\widehat{\varphi}_{k,r},\widehat{\rho}_{k,r,s}), \quad (28a)$$

$$\boldsymbol{\Omega}_2^{(t)} \triangleq \sum_{i\neq k}^{K}\sum_{r=1}^{R}\sum_{s=1}^{S} \Big\{\boldsymbol{u}(\widehat{\varphi}_{i,r},\widehat{\rho}_{i,r,s})\boldsymbol{u}^{\mathrm{H}}(\widehat{\varphi}_{i,r},\widehat{\rho}_{i,r,s}) - \frac{1}{N_{\mathrm{BS}}}\boldsymbol{I}_{N_{\mathrm{BS}}}\Big\}. \quad (28b)$$

The AoBF scheme based on imperfect CSI is summarized in Algorithm 2. The stop condition in step 14 is set as $\left\|[\boldsymbol{F}_{\mathrm{RF}}]_{:,k}^{(t)} - [\boldsymbol{F}_{\mathrm{RF}}]_{:,k}^{(t-1)}\right\|_2^2 \leq \epsilon$ or $t > T_{\max}$.

Algorithm 2 AoBF based on imperfect CSI

1: **Input:** N_{BS}, $\widetilde{p}_k$, $\widetilde{q}_k$, R, S, ω, ϵ, and $T_{\max}$.
2: **for** $k = 1 : K$ **do**
3: Initialize $[\boldsymbol{F}_{\mathrm{RF}}]_{:,k}^{(t)} = \boldsymbol{v}_{\widetilde{p}_k,\widetilde{q}_k}$, $t = 0$
4: **for** $r = 1 : R$ **do**
5: **for** $s = 1 : S$ **do**
6: Obtain $(\widehat{\varphi}_{k,r},\widehat{\rho}_{k,r,s})$ via Eqs. (24) and (25)
7: **end for**
8: **end for**
9: **repeat**
10: Obtain $\boldsymbol{\Omega}_1^{(t)}$ via Eq. (28a)
11: Obtain $\boldsymbol{\Omega}_2^{(t)}$ via Eq. (28b)
12: Obtain $[\boldsymbol{F}_{\mathrm{RF}}]_{:,k}^{(t+1)}$ via Eq. (27)
13: $t = t + 1$
14: **until** stop condition is satisfied
15: $[\boldsymbol{F}_{\mathrm{RF}}]_{:,k} = [\boldsymbol{F}_{\mathrm{RF}}]_{:,k}^{(t)}$
16: **end for**
17: **Output:** $\boldsymbol{F}_{\mathrm{RF}}$.

4 Simulation results

In this section, the performances of the proposed AoBF schemes are evaluated. For downlink transmission, a ULA with $N_{\mathrm{BS}} = 64$ antennas is equipped at the BS. The number of channel paths is set to be $L = 3$ for each UE. The complex-valued channel gains follow $\alpha_{k,1} \sim \mathcal{CN}(0,1)$ and $\alpha_{k,l} \sim \mathcal{CN}(0,0.01)$ for $l = 2,3$. There are $K = 4$ UEs served by the BS, and the locations of UEs and scatterers are randomly generated within the near field. Specifically, the angles follow a uniform distribution in $[-\pi/2,\pi/2)$, and the distances to the central point of the ULA are randomly generated within the Rayleigh distance D_{R}. The weight parameter of the MM method is set to be $\omega = 1000$. The parameters for the stop condition in Algorithms 1 and 2 are set to be $\epsilon = 10^{-9}$ and $T_{\max} = 1000$. For beam sweeping in the near field, the number of code words in the angle dimension is set to be $N_{\mathrm{BS}} = 64$, and the number of code words in the distance dimension is set to be $N_{\mathrm{DIS}} = 320$. The parameter of polar-domain near-field codebook $\boldsymbol{\mathcal{V}}$ is set to be $\beta_{\Delta} = 1.6$ (Cui and Dai, 2022). According to Fig. 4, the changing point of the auxiliary point number is 4. Thus, we set $R = 4$ and $S = 4$. Monte Carlo simulations are performed based on 2000 random channel implementations.

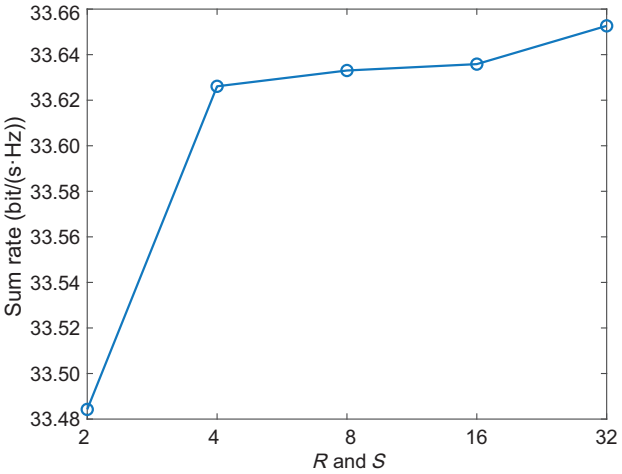


Fig. 4 The performance of AoBF based on imperfect CSI with different R and S. AoBF: analog-only beamforming; CSI: channel state information

4.1 Beam pattern comparison

Fig. 5 shows the beam patterns generated by analog-only beam steering, HBF with WMMSE-based digital beamforming, and our AoBF based on the perfect or imperfect CSI scheme. There are $K = 3$ UEs served by the BS. The locations of these UEs in polar coordinates are set to be $(-23.57°, 50\lambda)$, $(17.46°, 150\lambda)$, and $(-64.16°, 100\lambda)$. We set the first UE located at $(-23.57°, 50\lambda)$ as the target UE. As shown in Fig. 5, AoBF and HBF can mitigate multiuser interference by maximizing the power transmitted to the target UE via beam focusing and minimizing the power leaked to the other UEs via beam nulling in the near field. The normalized beam gains focused on the UEs are listed in Table 1. The beam gains from the BS to the target UE in the perfect-CSI-based schemes are close to 0 dB, since the beam can be accurately focused on the target UE with the help of perfect CSI. On the contrary, the beam gains from the BS to the target UE in the imperfect-CSI-based schemes are lower to about −2 dB, since the

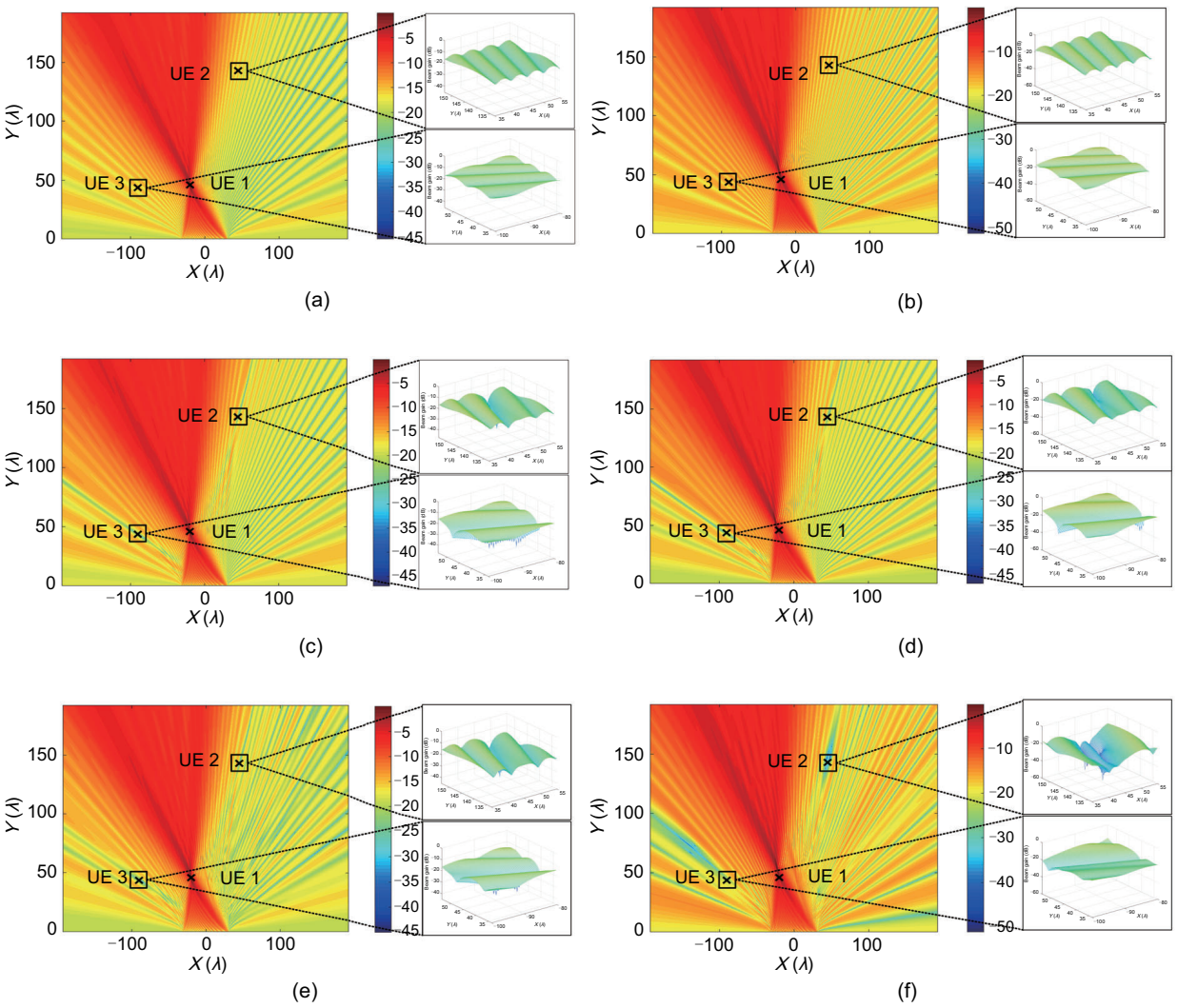


Fig. 5 Beam pattern comparison: (a) beam pattern generated by analog-only beam steering based on perfect CSI; (b) beam pattern generated by analog-only beam steering based on imperfect CSI; (c) beam pattern generated by HBF with WMMSE based on perfect CSI; (d) beam pattern generated by HBF with WMMSE based on imperfect CSI; (e) beam pattern generated by AoBF based on perfect CSI; (f) beam pattern generated by AoBF based on imperfect CSI. CSI: channel state information; HBF: hybrid beamforming; WMMSE: weighted minimum mean-squared error; AoBF: analog-only beamforming

Table 1 Normalized beam gain of each UE

Scheme	CSI	Beam gain (dB)		
		UE 1	UE 2	UE 3
Analog-only beam steering	Perfect	-7.5991×10^{-7}	–15.3376	–14.6842
Analog-only beam steering	Imperfect	–2.1414	–15.9440	–15.2837
AoBF	Perfect	–0.0105	–40.3274	–32.4819
AoBF	Imperfect	–2.1255	–31.3642	–21.0754
HBF-WMMSE	Perfect	–0.0130	–41.3534	–37.2225
HBF-WMMSE	Imperfect	–2.4056	–36.2031	–24.1222

AoBF: analog-only beamforming; HBF: hybrid beamforming; WMMSE: weighted minimum mean-squared error; CSI: channel state information; UE: user equipment

UE locations obtained by beam sweeping are inaccurate and the inaccurate beam focusing leads to gain loss. Based on perfect CSI, AoBF can achieve similar beam patterns to HBF. Based on imperfect CSI, owing to the generation of auxiliary points, the nearby power around the unimportant UEs is attenuated in AoBF. Thus, it appears as a null-beam region. These results intuitively indicate the effectiveness of our AoBF schemes for multiuser interference suppression via beam focusing and beam nulling.

4.2 Sum rate evaluation

In Fig. 6, the performance of AoBF is compared with those of analog-only beam steering (Alkhateeb et al., 2015), HBF with ZF-based digital beamforming, and HBF with WMMSE-based digital beamforming (Wu ZD and Dai, 2023) in the near field. The performance is evaluated in terms of the sum rate with different signal-to-noise ratios (SNRs). SNR is defined as $P\left|\boldsymbol{h}_k^{\mathrm{H}}[\boldsymbol{F}]_{:,k}\right|^2/(K\sigma^2)$. The number of UEs is set to be $K=4$. Particularly, the perfect-CSI-based schemes can be considered as the performance upper bounds. Based on the perfect CSI, the performances of our AoBF schemes can approach those of HBF-ZF and HBF-WMMSE. This implies the possibility of replacing HBF with AoBF. Based on imperfect CSI, HBF-WMMSE and HBF-ZF outperform AoBF since digital beamforming in HBF provides more degrees of freedom for beamforming compared with AoBF. Owing to the multiuser interference suppression ability of our AoBF schemes as shown in Figs. 5e and 5f, AoBF outperforms analog-only beam steering. For instance, based on imperfect CSI, AoBF can achieve 29.18% performance improvement over analog-only beam steering at SNR = 20 dB.

In Fig. 7, the performance of AoBF in the near field is compared with those of existing far-field schemes, including the far-field HBF-WMMSE scheme (Alkhateeb et al., 2015) and the far-field A-MM scheme (Qi et al., 2024). For a fair comparison, we extend the partially connected A-MM scheme (Qi et al., 2024) to the fully connected structure. The A-MM scheme is designed based on far-field modeling and a far-field codebook. Thus, it cannot distinguish UEs located at different distances in the near field. Our AoBF scheme is designed based on the near-field system model and codebook. The beamforming method is adjusted accordingly. The ability to distinguish UEs in AoBF is improved, owing to the introduction of the distance dimension. As shown in Fig. 8, AoBF can distinguish UEs located at the same angle and different distances. Thus, it can be seen in Fig. 7 that the near-field AoBF schemes perform slightly better than the far-field A-MM. The gap between AoBF and HBF-WMMSE in the near field is narrower than that between A-MM and HBF-WMMSE in the far field. At SNR = 20 dB, AoBF achieves 85.90% of the sum rate of HBF-WMMSE in the near field, while A-MM can achieve only 85.50% of the sum rate of HBF-WMMSE in the far field. Compared with far-field A-MM, better performance of near-field AoBF is achieved due to the extra degree of freedom in the distance dimension.

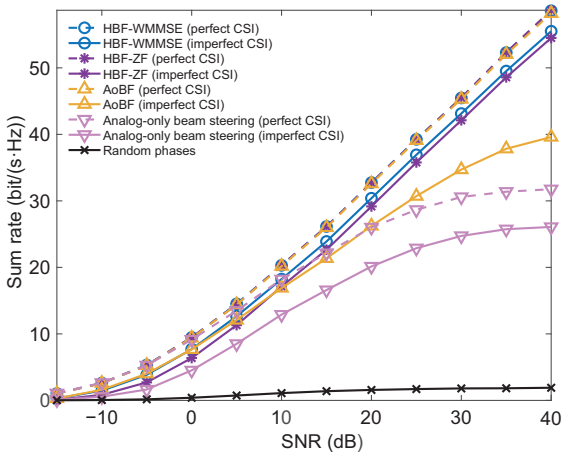


Fig. 6 Comparison of the proposed schemes with the existing schemes in terms of the sum rate for different signal-to-noise ratios (SNRs)

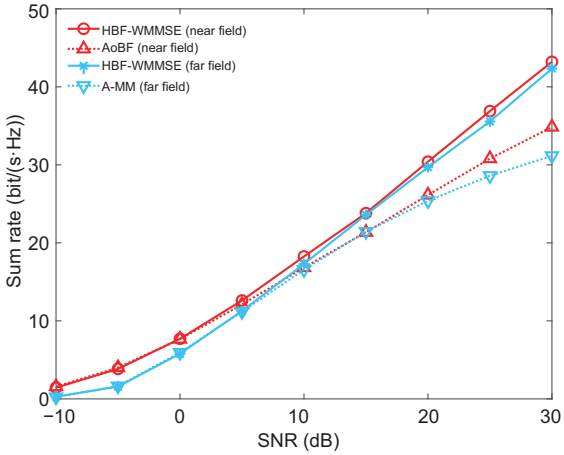


Fig. 7 Comparison of near-field and far-field schemes in terms of the sum rate for different signal-to-noise ratios (SNRs)

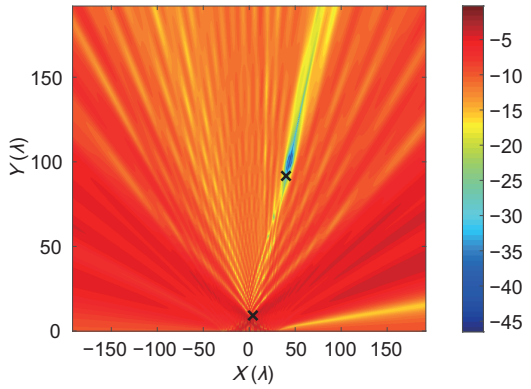


Fig. 8 Illustration of the beam pattern generated by imperfect-CSI-based AoBF if the UEs are located at the same angle in the near field. AoBF: analog-only beamforming; CSI: channel state information; UE: user equipment

In Fig. 9, we compare AoBF with the existing schemes in terms of the sum rate with different N_{BS}'s. In this simulation, the UE number is set to be $K = 4$, and the SNR is set to be 20 dB. It can be seen that the performances of all schemes are improved with the increase of N_{BS}. This is caused by two reasons. First, the ULA with more antennas generates more focused beams and, therefore, achieves larger beam gains. Second, the resolution of beam sweeping with a larger array is higher. The accuracy of the UE location from beam sweeping is improved, and the gap between imperfect CSI and perfect CSI is reduced with the increase of N_{BS}. Based on perfect CSI, the performances of AoBF and HBF are close. Thus, the gap between the AoBF and HBF schemes based on imperfect CSI becomes narrower with the increase of N_{BS}. Therefore, increasing the antenna number is an effective way to improve the performance of AoBF if the cost is permitted.

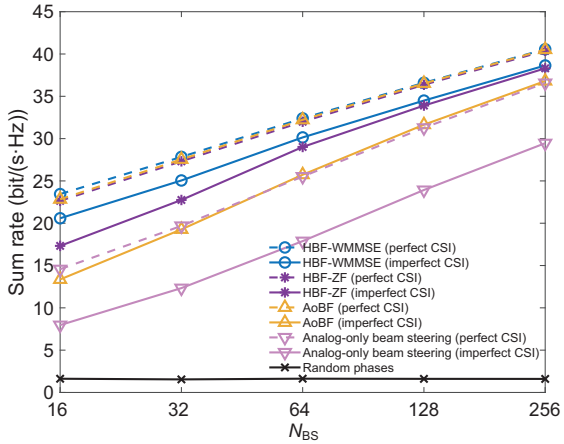


Fig. 9 Comparison of the proposed schemes with the existing schemes in terms of the sum rate for different N_{BS}'s

In Fig. 10, we compare AoBF with the existing schemes in terms of the sum rate and the averaged achievable rate $\sum_{k=1}^{K} R_k/K$ with different K's. In this simulation, the antenna number is set to be $N_{\mathrm{BS}} = 64$, and the SNR is set to be 20 dB. It can be seen that the sum rates of all schemes increase with the increase of K. The averaged achievable rates of these schemes decrease with the increase of K. The reason is that the interference among UEs becomes more severe with a larger K.

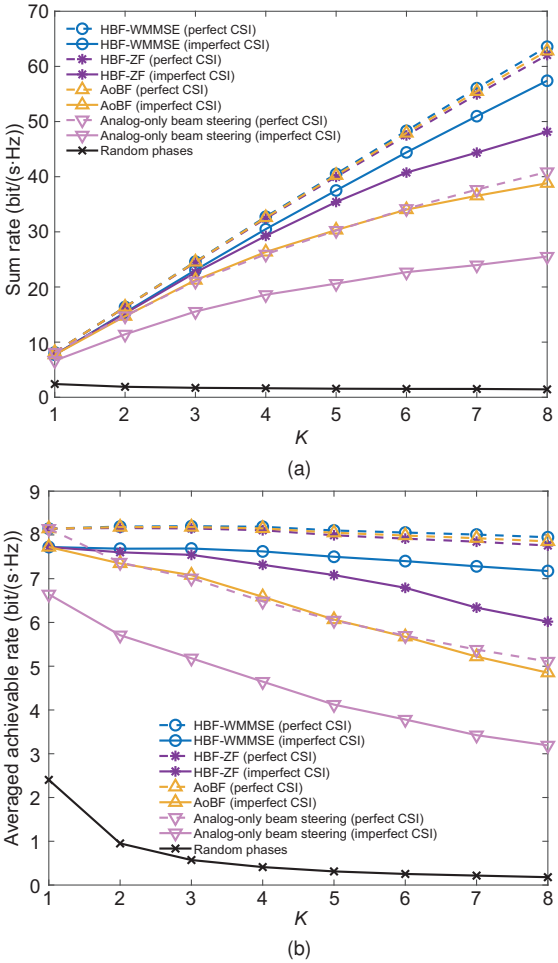


Fig. 10 Comparison of the proposed schemes with the existing schemes for different K's: (a) sum rate; (b) averaged achievable rate

4.3 Energy efficiency evaluation

Compared with HBF, AoBF removes the digital beamforming module and, therefore, can achieve system reconfiguration simplification and energy

efficiency improvement. The energy efficiency (EE) is defined as follows (Qi et al., 2022; Jin et al., 2024):

$$\mathrm{EE} \triangleq \sum_{k=1}^{K} R_k \Big/ P_{\mathrm{total}}, \tag{29}$$

where

$$P_{\mathrm{total}} \triangleq P + N_{\mathrm{RF}} P_{\mathrm{RF}} + N_{\mathrm{BS}} N_{\mathrm{RF}} P_{\mathrm{PS}} + P_{\mathrm{BB}}. \tag{30}$$

The variables P, P_{RF}, P_{PS}, and P_{BB} represent the power of the BS, each RF chain, each phase shifter, and digital beamforming in the baseband, respectively. We set $P_{\mathrm{RF}} = 26$ mW, $P_{\mathrm{PS}} = 10$ mW, and $P_{\mathrm{BB}} = 200$ mW (Mo et al., 2017; Yan et al., 2020).

As shown in Fig. 11, we compare AoBF with the existing schemes in terms of EE with different SNRs. Our AoBF schemes achieve better EE than the HBF schemes (Wu ZD and Dai, 2023), owing to the removal of the digital beamforming module. In addition, AoBF outperforms analog-only beam steering due to the higher sum rate achieved by multiuser interference suppression. Based on imperfect CSI, AoBF achieves 14.60% and 30.95% EE improvements over HBF-WMMSE and analog-only beam steering at SNR = 10 dB, respectively.

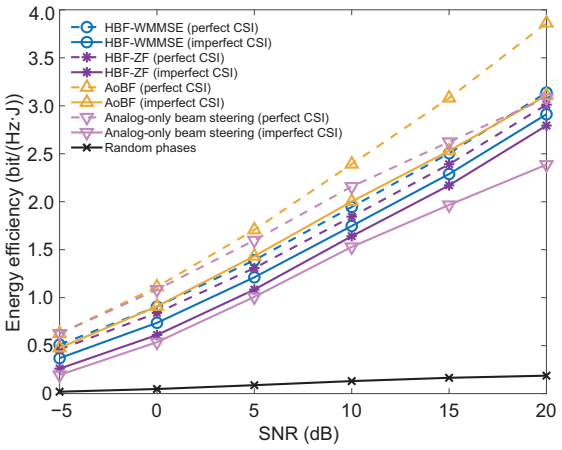


Fig. 11 Comparison of the proposed schemes with the existing schemes in terms of energy efficiency for different signal-to-noise ratios (SNRs)

5 Conclusions

In this study, we have proposed two AoBF schemes for multiuser near-field communications based on perfect CSI and imperfect CSI, separately. The proposed AoBF schemes can approach the performance of HBF with a simplified system configuration and higher EE. Future study will focus on the AoBF design based on physically consistent modeling.

Contributors

Ying WANG and Chenhao QI designed the research. Ying WANG processed the data and drafted the paper. Chenhao QI revised and finalized the paper.

Conflict of interest

Both authors declare that they have no conflict of interest.

Data availability

The data that support the findings of this study are available from the corresponding author upon reasonable request.

References

Ahmed I, Khammari H, Shahid A, et al., 2018. A survey on hybrid beamforming techniques in 5G: architecture and system model perspectives. *IEEE Commun Surv Tut*, 20(4):3060-3097. https://doi.org/10.1109/COMST.2018.2843719

Alkhateeb A, Leus G, Heath RW, 2015. Limited feedback hybrid precoding for multi-user millimeter wave systems. *IEEE Trans Wirel Commun*, 14(11):6481-6494. https://doi.org/10.1109/TWC.2015.2455980

Cao P, Thompson JS, Haas H, 2017. Constant modulus shaped beam synthesis via convex relaxation. *IEEE Antenn Wirel Propag Lett*, 16:617-620. https://doi.org/10.1109/LAWP.2016.2594141

Chen KJ, Qi CH, Li GY, et al., 2024. Near-field multiuser communications based on sparse arrays. *IEEE J Sel Top Signal Process*, 18(4):619-632. https://doi.org/10.1109/JSTSP.2024.3416681

Cui MY, Dai LL, 2022. Channel estimation for extremely large-scale MIMO: far-field or near-field? *IEEE Trans Commun*, 70(4):2663-2677. https://doi.org/10.1109/TCOMM.2022.3146400

Cui MY, Dai LL, 2024. Near-field wideband beamforming for extremely large antenna arrays. *IEEE Trans Wirel Commun*, 23(10):13110-13124. https://doi.org/10.1109/TWC.2024.3398770

Gong SQ, Xing CW, Lau VKN, et al., 2020. Majorization-minimization aided hybrid transceivers for MIMO interference channels. *IEEE Trans Signal Process*, 68:4903-4918. https://doi.org/10.1109/TSP.2020.3018548

Gong TR, Gavriilidis P, Ji R, et al., 2024a. Holographic MIMO communications: theoretical foundations, enabling technologies, and future directions. *IEEE Commun Surv Tut*, 26(1):196-257. https://doi.org/10.1109/COMST.2023.3309529

Gong TR, Wei L, Huang CW, et al., 2024b. Holographic MIMO communications with arbitrary surface placements: near-field LoS channel model and capacity limit. *IEEE J Sel Areas Commun*, 42(6):1549-1566. https://doi.org/10.1109/JSAC.2024.3389126

Gong TR, Wei L, Huang CW, et al., 2024c. Near-field channel modeling for holographic MIMO communications. *IEEE Wirel Commun*, 31(3):108-116. https://doi.org/10.1109/MWC.005.2300457

Jin X, Lv TJ, Ni W, et al., 2024. A reconfigurable subarray architecture and hybrid beamforming for millimeter-wave dual-function-radar-communication systems. *IEEE Trans Wirel Commun*, 23(10):12594-12607. https://doi.org/10.1109/TWC.2024.3393739

Li LC, Pan CH, Zhi KD, et al., 2024. Transmission design for the XL-RIS-aided massive MIMO system with visibility regions. *Front Inform Technol Electron Eng*, 25(12):1679-1694. https://doi.org/10.1631/FITEE.2400375

Liu Y, Xu K, Xia XC, et al., 2023. Joint power control and passive beamforming optimization in RIS-assisted anti-jamming communication. *Front Inform Technol Electron Eng*, 24(12):1791-1802. https://doi.org/10.1631/FITEE.2200646

Mo JH, Alkhateeb A, Abu-Surra S, et al., 2017. Hybrid architectures with few-bit ADC receivers: achievable rates and energy-rate tradeoffs. *IEEE Trans Wirel Commun*, 16(4):2274-2287. https://doi.org/10.1109/TWC.2017.2661749

Qi CH, Liu Q, Yu XH, et al., 2022. Hybrid precoding for mixture use of phase shifters and switches in mmWave massive MIMO. *IEEE Trans Commun*, 70(6):4121-4133. https://doi.org/10.1109/TCOMM.2022.3173304

Qi CH, Hu JL, Du Y, et al., 2024. Multiuser beamforming for partially-connected millimeter wave massive MIMO. *IEEE Trans Veh Technol*, 73(4):5977-5981. https://doi.org/10.1109/TVT.2023.3331713

Shen Y, Leng PF, Chen SY, et al., 2024. Phase-only transmit beampattern synthesis with maximum mainlobe gain via manifold ADMM. *IEEE Antenn Wirel Propag Lett*, 23(1):184-188. https://doi.org/10.1109/LAWP.2023.3321021

Sherman J, 1962. Properties of focused apertures in the Fresnel region. *IRE Trans Antenn Propag*, 10(4):399-408. https://doi.org/10.1109/TAP.1962.1137900

Song JX, Babu P, Palomar DP, 2015. Optimization methods for designing sequences with low autocorrelation sidelobes. *IEEE Trans Signal Process*, 63(15):3998-4009. https://doi.org/10.1109/TSP.2015.2425808

Sun XY, Qi CH, Li GY, 2019. Beam training and allocation for multiuser millimeter wave massive MIMO systems. *IEEE Trans Wirel Commun*, 18(2):1041-1053. https://doi.org/10.1109/TWC.2018.2889071

Sun Y, Babu P, Palomar DP, 2017. Majorization-minimization algorithms in signal processing, communications, and machine learning. *IEEE Trans Signal Process*, 65(3):794-816. https://doi.org/10.1109/TSP.2016.2601299

Tian Z, Chen ZC, Wang M, et al., 2022. Reconfigurable intelligent surface empowered optimization for spectrum sharing: scenarios and methods. *IEEE Veh Technol Mag*, 17(2):74-82. https://doi.org/10.1109/MVT.2022.3157070

Tian Z, Yao Y, Chen ZC, et al., 2024. Active reconfigurable intelligent surface-aided user-centric networks. *IEEE Trans Veh Technol*, 73(2):2930-2935. https://doi.org/10.1109/TVT.2023.3318979

Wang J, Sun JY, Fang W, et al., 2024. Deep reinforcement learning for near-field wideband beamforming in STAR-RIS networks. *Front Inform Technol Electron Eng*, 25(12):1651-1663. https://doi.org/10.1631/FITEE.2400364

Wang XH, Shu F, Chen RQ, et al., 2023. Beamforming design for RIS-aided amplify-and-forward relay networks. *Front Inform Technol Electron Eng*, 24(12):1728-1738. https://doi.org/10.1631/FITEE.2300118

Wu LL, Babu P, Palomar DP, 2018. Transmit waveform/receive filter design for MIMO radar with multiple waveform constraints. *IEEE Trans Signal Process*, 66(6):1526-1540. https://doi.org/10.1109/TSP.2017.2787115

Wu ZD, Dai LL, 2023. Multiple access for near-field communications: SDMA or LDMA? *IEEE J Sel Areas Commun*, 41(6):1918-1935. https://doi.org/10.1109/JSAC.2023.3275616

Yan LF, Han C, Yuan JH, 2020. A dynamic array-of-subarrays architecture and hybrid precoding algorithms for terahertz wireless communications. *IEEE J Sel Areas Commun*, 38(9):2041-2056. https://doi.org/10.1109/JSAC.2020.3000876

Yang LJ, Sun S, Sha WEI, et al., 2023. Multi-feed multi-mode metasurface for independent orbital angular momentum communication in dual polarization. *Front Inform Technol Electron Eng*, 24(12):1776-1790. https://doi.org/10.1631/FITEE.2200471

Yoon SG, Lee SJ, 2022. Improved hierarchical codebook-based channel estimation for mmWave massive MIMO systems. *IEEE Wirel Commun Lett*, 11(10):2095-2099. https://doi.org/10.1109/LWC.2022.3193877

You CS, Zhang R, 2021. Wireless communication aided by intelligent reflecting surface: active or passive? *IEEE Wirel Commun Lett*, 10(12):2659-2663. https://doi.org/10.1109/LWC.2021.3111044

Zhang HY, Shlezinger N, Guidi F, et al., 2022. Beam focusing for near-field multiuser MIMO communications. *IEEE Trans Wirel Commun*, 21(9):7476-7490. https://doi.org/10.1109/TWC.2022.3158894

Zhang HY, Shlezinger N, Guidi F, et al., 2023. 6G wireless communications: from far-field beam steering to near-field beam focusing. *IEEE Commun Mag*, 61(4):72-77. https://doi.org/10.1109/MCOM.001.2200259